PHYSICAL REVIEW D **71,** 024027 (2005)

Dynamics of precessing binary black holes using the post-Newtonian approximation

Michael D. Hartl
Theoretical Astrophysics, 130-33 Caltech, Pasadena, California 91125, USA

Alessandra Buonanno
groupe de Gravitation et Cosmologie (GReCO), Institut d'Astrophysique de Paris (CNRS), 98 Boulevard Arago, 75014 Paris, France
(Received 23 July 2004; published 24 January 2005)

We investigate the (conservative) dynamics of binary black holes using the Hamiltonian formulation of the post-Newtonian (PN) equations of motion. The Hamiltonian we use includes spin-orbit coupling, spin-spin coupling, and mass monopole/spin-induced quadrupole interaction terms. We investigate the qualitative effects of these terms on the orbits; in the case of both quasicircular and eccentric orbits, we search for the presence of chaos (using the method of Lyapunov exponents) for a large variety of initial conditions. For quasicircular orbits, we find no chaotic behavior for black holes with total mass $10–40M_\odot$ when initially at a separation corresponding to a Newtonian gravitational-wave (GW) frequency less than $\sim$150 Hz. Only for rather small initial radial distances (corresponding to a GW frequency larger than $\sim$150 Hz), for which spin-spin induced oscillations in the radial separation are rather important, do we find chaotic solutions, and even then they are rare. Moreover, these chaotic quasicircular orbits are of questionable astrophysical significance, since they originate from direct parametrization of the equations of motion rather than from widely separated binaries evolving to small separations under gravitational radiation reaction. In the case of highly eccentric orbits, which for ground-based interferometers are not astrophysically favored, we again find chaotic solutions, but only at pericenters so small that higher order PN corrections, especially higher spin PN corrections, should also be taken into account. Taken together, our surveys of quasicircular and eccentric orbits find chaos only for orbits that are either of dubious astrophysical interest for ground-based interferometers or which violate the approximations required for the equations of motion to be physically valid at the post-Newtonian order considered.

DOI: 10.1103/PhysRevD.71.024027 PACS numbers: 04.70.Bw, 04.80.Nn, 95.10.Fh

I. INTRODUCTION

Relativistic binary systems made of compact objects, such as neutron stars or black holes, are among the most promising (or, at least, are among the best-understood) candidates for the production of gravitational waves detectable by both ground- and space-based gravitational-wave observatories. The difficulty of detecting the signals from such systems has led to a theoretical effort to understand the gravitational waveforms likely to be emitted by such systems, which in turn has led to a consideration of their dynamical behavior. In particular, several authors [1–5] have investigated the presence of chaos in the dynamics of compact binaries, motivated in part by the effect of such chaos on the calculation of theoretical templates for use in matched filters. The extreme sensitivity on initial conditions that characterizes chaotic systems would lead to significant difficulties in the implementation of such filters, since the number of filters would grow exponentially with increasing detection sensitivity.

In the extreme mass-ratio limit, chaos was found in the equations describing a *spinning* particle orbiting a nonrotating (Schwarzschild) black hole [1]. References [5,6] extended this result to the case of a rotating (Kerr) black hole, finding widespread chaotic solutions. As demonstrated in [5], however, the values of the total spin for the test particle leading to chaotic solutions are not realizable in physical systems. Furthermore, [6] showed that chaos, while widespread for these unrealistic spin values, disappears in all cases for physically realistic spins. In short, there is strong evidence that extreme mass-ratio systems, which are most relevant for proposed space-based gravitational-wave detectors, are not chaotic for any parameter values of physical interest.

The case of the comparable-mass binaries more relevant to ground-based gravitational-wave observatories has been investigated by several authors [2–4] using the post-Newtonian (PN) equations of motion in the Lagrangian formalism, using harmonic gauge [7,8]. There was initially some doubt regarding the results presented in [2], which found chaos in the PN equations for spinning bodies, since the time scale of the chaos was not reported: it was not clear whether the chaos discovered in the equations—in the conservative limit neglecting gravitational radiation reaction—would have time to manifest itself in the inspiral time scale $t_{\rm insp}$. Furthermore, the work in [3] cast doubt on the presence of chaos in these systems, finding that the Lyapunov characteristic exponents for the PN equations, which measure the divergence rate of nearby trajectories, are zero in all cases tested. However, [4] found some initial conditions, corresponding to rather eccentric orbits, that do have positive Lyapunov exponents, indicating the presence of chaos, with characteristic times shorter than $t_{\rm insp}$, raising

the possibility that theoretical templates calculated for systems with spinning compact objects are affected by chaos.

In the present study, we examine and extend these results by investigating the dynamics of spinning binary black holes using a Hamiltonian formulation of the post-Newtonian equations of motion [9–13] in the Arnowitt-Deser-Misner (ADM) gauge. In order to make chaos formally possible, we exclude gravitational radiation reaction; since tests for chaos technically require an infinite-time limit, the finite inspiral times due to radiation reaction would eliminate the possibility of chaos. On the other hand, we do include post-Newtonian terms involving the spin of the two bodies: the addition of spin is essential to create the possibility of chaos, since without spin the constants of the motion constrain the motion to be at most quasiperiodic. As discussed in Sec. II A, we use four separate spin terms in the equations of motion to model accurately their effect of the dynamics. We focus on black holes, to the exclusion of other compact astrophysical objects, because two of these spin terms (which involve spin quadrupole effects) are known exactly only for black holes, and yet their magnitudes are comparable to the spin-spin coupling and hence cannot be ignored. (This is an extension of previous work, as other authors have not considered these quadrupole terms when investigating chaos.)

In Sec. II we write down the PN Hamiltonian, including spin terms, and in Sec. III we discuss how we choose initial conditions for quasicircular and eccentric orbits. We then investigate chaos for comparable-mass binary black holes (Sec. IV). Since binary black hole inspirals tend to *circularize* under gravitational radiation reaction, we focus first on the important special case of *quasicircular* orbits and then analyze eccentric orbits. As in previous work, we favor Lyapunov exponents (Sec. IV A) to quantify the presence (or absence) of chaos.

We work almost exclusively in geometric units ($G = c = 1$). Euclidean vectors, such as appear in the post-Newtonian equations of motion, are set in boldface, and we use vector arrows to denote relativistic 4-vectors. The symbol log refers in all cases to the natural logarithm.

II. THE POST-NEWTONIAN EQUATIONS OF MOTION

The post-Newtonian equations for the two-body problem are an approximation to full general relativity, essentially involving a series expansion in v/c. As in the case of the classical two-body problem, in the post-Newtonian case it is possible to describe the motion of a relativistic binary in the center-of-mass frame. A typical orbit is shown in Fig. 1. In this paper, we use the center-of-mass Hamiltonian, as developed in Refs. [9–13]. The Hamiltonian formulation is particularly convenient for our present purposes: since detecting chaos involves determining the separation of nearby *phase-space* trajectories, it is convenient to work directly in terms of spatial coordinates and their corresponding conjugate momenta—a criterion automatically satisfied by the Hamiltonian formulation.

A. The Hamiltonian formulation

We can represent the PN Hamiltonian schematically as follows:

$$H = H_{\rm N} + H_{\rm PN} + H_{\rm SO} + H_{\rm SS}. \tag{2.1}$$

We include the following terms: Newtonian, post-Newtonian (usually through 2PN order, i.e., v^4/c^4, and sometimes through 3PN order, i.e., v^6/c^6), spin-orbit coupling (through 1.5PN order), and spin-spin coupling

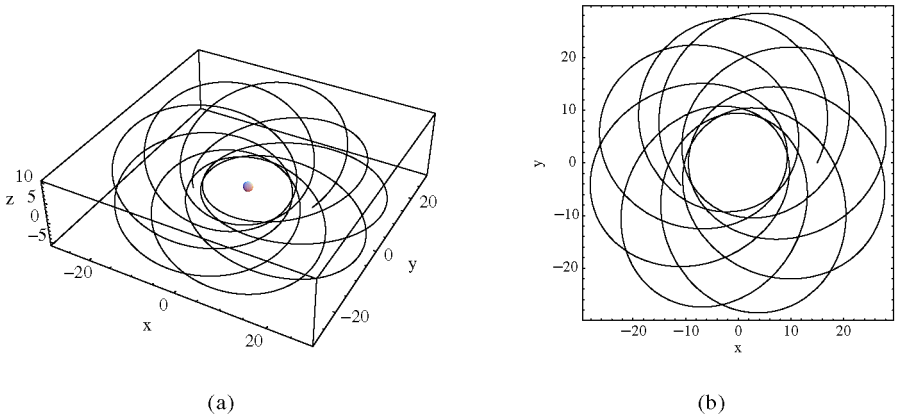

FIG. 1 (color online). The orbit of two maximally spinning $10M_\odot$ black holes, using a Hamiltonian formulation of the post-Newtonian equations of motion. (a) The orbit embedded in Euclidean space; (b) the projection onto the x-y plane. Lengths are measured in terms of the total mass $M = m_1 + m_2$, and we show a schematic horizon at $r_{\rm H} = M$, indicating the collapse radius where the relative separation of the two bodies is the sum of their horizon radii. (We have $r_{\rm H,1} = m_1$, and $r_{\rm H,2} = m_2$ for maximally spinning black holes, so the relative separation of collapse is $r_{\rm H} = m_1 + m_2 = M$.) Note that, in contrast to Newtonian orbits, the orbit is not closed, and the orbital plane precesses around the center of mass.

(through 2PN order). (We omit the radiation reaction, as discussed in the introduction.) Throughout this treatment, we use $\mathbf{X}$ for the (relative) position, $\mathbf{P}$ for the conjugate (relative) momentum, and $(\mathbf{S}_1, \mathbf{S}_2)$ for the spins of the two objects.

We denote with m_1 and m_2 the mass of the two bodies, and introduce the total mass $M = m_1 + m_2$ and the reduced mass $\mu = m_1 m_2/M$.[1] Using these mass variables, we can express the first term (the standard Newtonian energy) as follows:

$$H_{\rm N} = \frac{P^2}{2\mu} - \frac{\mu M}{r}, \tag{2.2}$$

where $r = |\mathbf{X}|$. The post-Newtonian terms used in this paper are 1PN and 2PN (and, in some sections, 3PN), given by [9–13]:

$$H_{\rm PN} = \mu(\hat{H}_{\rm 1PN} + \hat{H}_{\rm 2PN} + \hat{H}_{\rm 3PN}), \tag{2.3}$$

where

$$\hat{H}_{\rm 1PN} = \frac{1}{8}(3\eta - 1)(\mathbf{p}^2)^2 - \frac{1}{2}[(3+\eta)\mathbf{p}^2 + \eta(\mathbf{n}\cdot\mathbf{p})^2]\frac{1}{q} + \frac{1}{2q^2} \tag{2.4}$$

and

$$\hat{H}_{\rm 2PN} = \frac{1}{16}(1 - 5\eta + 5\eta^2)(\mathbf{p}^2)^3 + \frac{1}{8}[(5 - 20\eta - 3\eta^2) \times (\mathbf{p}^2)^2 - 2\eta^2(\mathbf{n}\cdot\mathbf{p})^2\mathbf{p}^2 - 3\eta^4(\mathbf{n}\cdot\mathbf{p})^4]\frac{1}{q} + \frac{1}{2}[(5+8\eta)(\mathbf{p}^2) + 3\eta(\mathbf{n}\cdot\mathbf{p})^2]\frac{1}{q^2} - \frac{1}{4}(1+3\eta)\frac{1}{q^3} \tag{2.5}$$

and

$$\hat{H}_{\rm 3PN}(\mathbf{q},\mathbf{p}) = \frac{1}{128}(-5 + 35\eta - 70\eta^2 + 35\eta^3)(\mathbf{p}^2)^4 + \frac{1}{16}[(-7 + 42\eta - 53\eta^2 - 5\eta^3)(\mathbf{p}^2)^3 + (2 - 3\eta)\eta^2(\mathbf{n}\cdot\mathbf{p})^2(\mathbf{p}^2)^2 + 3(1-\eta)\eta^2(\mathbf{n}\cdot\mathbf{p})^4\mathbf{p}^2 - 5\eta^3(\mathbf{n}\cdot\mathbf{p})^6]\frac{1}{q} + \left[\frac{1}{16}(-27 + 136\eta + 109\eta^2)(\mathbf{p}^2)^2 + \frac{1}{16}(17 + 30\eta)\eta(\mathbf{n}\cdot\mathbf{p})^2\mathbf{p}^2 + \frac{1}{12}(5 + 43\eta)\eta(\mathbf{n}\cdot\mathbf{p})^4\right]\frac{1}{q^2} + \left\{\left[-\frac{25}{8} + \left(\frac{1}{64}\pi^2 - \frac{335}{48}\right)\eta - \frac{23}{8}\eta^2\right]\mathbf{p}^2 + \left(-\frac{85}{16} - \frac{3}{64}\pi^2 - \frac{7}{4}\eta\right)\eta(\mathbf{n}\cdot\mathbf{p})^2\right\}\frac{1}{q^3} + \left[\frac{1}{8} + \left(\frac{109}{12} - \frac{21}{32}\pi^2\right)\eta\right]\frac{1}{q^4}. \tag{2.6}$$

In the preceding formulas, we have $\eta = m_1 m_2/M^2$, and we use the unit vector $\mathbf{n} = \mathbf{X}/r$ and the reduced canonical variables $\mathbf{p} = \mathbf{P}/\mu$ and $\mathbf{q} = \mathbf{X}/M$. In most of this paper, we will measure momenta in terms of μ and distances in terms of M, so we will typically not distinguish between the canonical and reduced canonical variables. In this paper, in $H_{\rm PN}$ we use only the terms through the 2PN corrections (thereby omitting the 3PN terms) except where explicitly noted.

The next term in Eq. (2.1) is the spin-orbit coupling (corresponding to Lense-Thirring precession in the extreme mass-ratio limit $m_2 \gg m_1$):

$$H_{\rm SO} = \frac{\mathbf{L}\cdot\mathbf{S}_{\rm eff}}{r^3}, \tag{2.7}$$

where

$$\mathbf{S}_{\rm eff} = \left(2 + \frac{3}{2}\frac{m_2}{m_1}\right)\mathbf{S}_1 + \left(2 + \frac{3}{2}\frac{m_1}{m_2}\right)\mathbf{S}_2. \tag{2.8}$$

The spin-coupling term in Eq. (2.1) has three components:

$$H_{\rm SS} = H_{\rm S_1S_2} + H_{\rm S_1S_1} + H_{\rm S_2S_2}. \tag{2.9}$$

The first term, the spin-spin coupling, is

$$H_{\rm S_1S_2} = \frac{1}{r^3}[3(\mathbf{S}_1\cdot\mathbf{n})(\mathbf{S}_2\cdot\mathbf{n}) - \mathbf{S}_1\cdot\mathbf{S}_2], \tag{2.10}$$

which is valid for all bodies (e.g., neutron stars or white dwarfs). The next two terms we include are monopole-quadrupole interaction terms, and their form is valid only for black holes.[2] They are [14,15]

$$H_{\rm S_1S_1} = \frac{1}{2r^3}[3(\mathbf{S}_1\cdot\mathbf{n})(\mathbf{S}_1\cdot\mathbf{n}) - \mathbf{S}_1\cdot\mathbf{S}_1]\frac{m_2}{m_1} \tag{2.11}$$

and

$$H_{\rm S_2S_2} = \frac{1}{2r^3}[3(\mathbf{S}_2\cdot\mathbf{n})(\mathbf{S}_2\cdot\mathbf{n}) - \mathbf{S}_2\cdot\mathbf{S}_2]\frac{m_1}{m_2}. \tag{2.12}$$

With the full Hamiltonian in hand, we can now derive the equations of motion using Poisson brackets. As in classical Hamiltonian mechanics, the time-evolution of a dynamical quantity $f(\mathbf{X}, \mathbf{P}, \mathbf{S}_1, \mathbf{S}_2)$ is simply the Poisson

[1] For clarity in what follows, we adopt the arbitrary convention that $m_1 \geq m_2$.

[2] We leave the generalization to neutron stars and other compact bodies to future work.

bracket of the quantity with the Hamiltonian:

$$\frac{df}{dt} = \{f, H\}. \tag{2.13}$$

The Hamiltonian equations of motion for the (relative) position and (relative) momentum are then the familiar canonical equations:

$$\frac{d\mathbf{X}}{dt} = +\frac{\partial H}{\partial \mathbf{P}}, \qquad \frac{d\mathbf{P}}{dt} = -\frac{\partial H}{\partial \mathbf{X}}. \tag{2.14}$$

To derive the spin equations of motion, we use the canonical angular momentum Poisson bracket

$$\{S^i, S^j\} = \epsilon^{ijk} S^k, \tag{2.15}$$

which yields

$$\frac{d\mathbf{S}_1}{dt} = \frac{\partial H}{\partial \mathbf{S}_1} \times \mathbf{S}_1 \equiv \Omega_1 \times \mathbf{S}_1 \tag{2.16}$$

and

$$\frac{d\mathbf{S}_2}{dt} = \frac{\partial H}{\partial \mathbf{S}_2} \times \mathbf{S}_2 \equiv \Omega_2 \times \mathbf{S}_2. \tag{2.17}$$

Equations (2.14) and (2.16) and (2.17), with the Hamiltonian given by Eq. (2.1), are the equations of motion used throughout this paper.

B. Conserved quantities

There are many conserved quantities in the post-Newtonian equations. These constants of the motion constrain the dynamical behavior of the system and provide valuable checks when testing a numerical implementation of the equations. Here we discuss all the quantities known to be conserved, and at which orders they are conserved.

1. Quantities conserved at all orders

The following quantities are conserved at all orders:

(i) Total energy H: $\dot{H} = \{H, H\} = 0$ by the antisymmetry of Poisson brackets.
(ii) Total angular momentum $\mathbf{J} = \mathbf{L} + \mathbf{S}_1 + \mathbf{S}_2$: see [15].
(iii) The spin magnitudes S_1 and S_2: this is evident from Eqs. (2.16) and (2.17), since the cross product is perpendicular to the spin and hence can change only its direction.

2. Quantities conserved only through spin-orbit coupling

If we neglect the terms quadratic in the spin (i.e., we include only terms through spin-orbit coupling), the following additional quantities are conserved:

(i) $L^2 = \mathbf{L} \cdot \mathbf{L}$: at this order, $\dot{\mathbf{L}} = \mathbf{S}_{\rm eff} \times \mathbf{L}/r^3$, which changes the direction of $\mathbf{L}$ but not its magnitude.
(ii) $\mathbf{L} \cdot \mathbf{S}_{\rm eff}$: see [15].

In our numerical implementation, we verify that the above quantities are conserved at the proper orders—that is, we check that energy, total angular momentum, and the spin magnitudes are always conserved, and verify that L and $\mathbf{L} \cdot \mathbf{S}_{\rm eff}$ are conserved when including only terms through spin-orbit coupling. To calculate the Lyapunov exponents we use the techniques and routines described in Chapter 5 of [16]. For more details on our numerical implementation, see the appendix.

III. PARAMETRIZING POST-NEWTONIAN ORBITS

We discuss here two convenient methods for parametrizing initial conditions for post-Newtonian orbits. We first describe a method that gives orbits that approximately satisfy desired values of eccentricity, pericenter, and orbital inclination. We then treat the important special case of quasicircular orbits. Finally, we examine the effects of varying the post-Newtonian terms included in the Hamiltonian.

A. Eccentric orbits

One convenient method for fixing initial conditions starts with the eccentricity e and pericenter r_p, which allows for the easy creation of bound orbits and makes contact with the Newtonian limit. For a Newtonian orbit with given values of (e, r_p), we can calculate the corresponding (reduced) angular momentum $L_{\rm N}$ and energy $E_{\rm N}$ using

$$L_{\rm N} = \sqrt{(1+e) r_p} \tag{3.1}$$

and

$$E_{\rm N} = 1 - \frac{1-e}{2r_p}, \tag{3.2}$$

where we have included the rest energy in the energy term. Our parametrization method then involves finding a post-Newtonian orbit with the same energy $E_{\rm N}$ as the Newtonian orbit, with the canonical momentum p_ϕ set equal to $L_{\rm N}$.[3]

The details of the eccentricity parametrization involve first setting $\mathbf{X}_0 = (r_p, 0, 0)$ and $p_r = 0$. We then set $p_\phi = L_{\rm N}/r$ (the Newtonian value of the ϕ momentum), leaving only p_θ undetermined. At this point we could set $p_\theta = 0$, in agreement with the Newtonian value; this choice leads to perfectly valid initial conditions. But, since we are studying the dynamics of a Hamiltonian system, we wish to assign a privileged role to the energy, and the choice $p_\theta = 0$ does not lead to a post-Newtonian system with the energy calculated from Eq. (3.2). Hence, we force the energies to agree using

[3]We use lowercase for p_ϕ (the canonical momentum conjugate to ϕ) to distinguish it from $P_\phi = \hat{\boldsymbol{\phi}} \cdot \mathbf{P}$, the ϕ component of $\mathbf{P}$.

$$H = E_{\mathrm{N}}, \tag{3.3}$$

which gives a sixth-degree polynomial equation in p_θ. Since the Newtonian value of p_θ is exactly zero, in order to produce the post-Newtonian orbit analogous to its Newtonian counterpart we choose the real root of Eq. (3.3) closest to zero. (This choice still leaves two roots, corresponding to initial values of p_θ in the $\pm z$ direction. We arbitrarily choose the negative root, so p_θ is initially in the $+z$ direction.)

We should note that the conditions $\mathbf{X}_0 = (r_p, 0, 0)$ and $p_r = 0$, which are chosen for computational convenience, mean that the initial orbit has its pericenter in the x-y plane, but this condition is not true for a generic post-Newtonian orbit; as a result, the initial conditions do not necessarily satisfy the requirements for a valid post-Newtonian orbit (particularly for the nonrotating case in which orbits are confined to a plane). Fortunately, as soon as the orbit reaches the true pericenter—that is, when p_r is again 0—*those* initial conditions do result in a valid post-Newtonian orbit. (This means that the radius of the pericenter *requested*—i.e., r_p—and the *empirical* pericenter differ, but by examining the numerical solutions we find that the requested and empirical pericenters typically differ by only a few percent.) Since no finite segment of the orbit can affect the presence of chaos, which is defined as an asymptotic property of the system (Sec. IVA), the small invalid piece at the beginning of the orbit does not affect the final result.

As a result of this parametrization method, we are able to find valid solutions to the post-Newtonian equations of motion that have empirical values of e and r_p (as determined by examining the numerical solution directly) quite close to the values of corresponding Newtonian orbits (Fig. 2).

B. Quasicircular orbits

A second, more specialized parametrization of the PN initial conditions enforces the condition of *quasicircularity*. In particular, through third post-Newtonian order the quasicircular orbits are in fact exactly circular, and even with spin-orbit coupling added there exist "spherical" orbits, i.e., orbits confined to lie on a sphere, with fixed radius but varying angle θ. Once any of the spin-spin terms is turned on, exact sphericity is impossible in general, but it is still possible to satisfy exactly the conditions leading to spherical orbits in the absence of spin-spin coupling. These orbits are especially important for modeling possible sources of gravitational radiation, since the orbits of compact binaries are expected to circularize due to gravitational radiation reaction [17].

The conditions leading to quasicircular orbits are as follows. Given an initial radius r_0, we set $\phi_0 = 0$ and $\theta_0 = \pi/2$, so that

$$\mathbf{X}_0 = (r_0, 0, 0). \tag{3.4}$$

We then require that the initial radial momentum vanish:

$$(P_r)_0 = 0. \tag{3.5}$$

[Since the Hamiltonian is quadratic in P_r, this means that $(\dot{r})_0 = (\partial H/\partial P_r)_{P_r=0} = 0$, so that (at least initially) the radius is not changing.] Finally, we require that the initial values of $\dot{P}_r$ and $\dot{\theta}$ vanish, which means (using Hamilton's equations) that

$$\left(\frac{dP_r}{dt}\right)_0 = -\left(\frac{\partial H}{\partial r}\right)_0 = 0 \tag{3.6}$$

and

$$\left(\frac{d\theta}{dt}\right)_0 = -\left(\frac{\partial H}{\partial P_\theta}\right)_0 = 0. \tag{3.7}$$

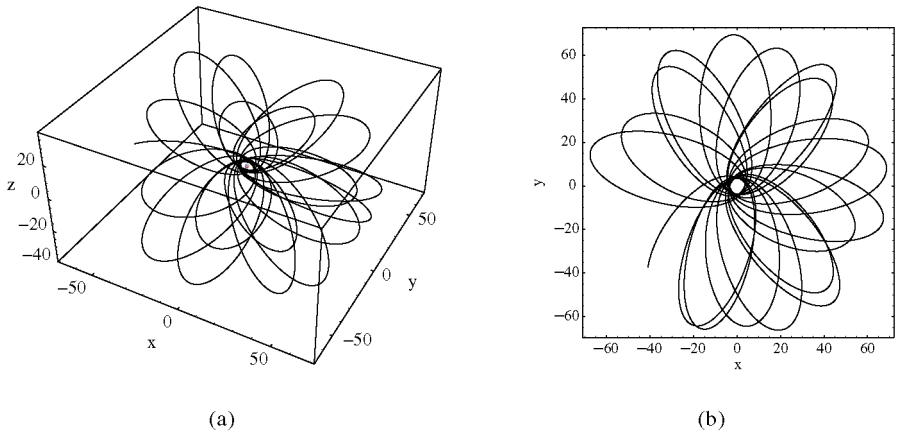

(a) (b)

FIG. 2 (color online). A highly eccentric orbit for two maximally spinning $10M_\odot$ black holes. (a) The orbit embedded in Euclidean space; (b) the projection onto the x-y plane. Lengths are measured in terms of the total mass $M = m_1 + m_2$, and we show a schematic horizon at $r_{\mathrm{H}} = M$. The energy and angular momentum of the orbit correspond to a Newtonian orbit with eccentricity $e = 0.9$, pericenter $r_p = 3.7M$. The empirical values of these parameters, as determined from the numerical solution to the equations of motion, are $e = 0.899$ and $r_p = 3.7M$. The spins are $S_1 = (1/\sqrt{2}, 0, 1/\sqrt{2})$ and $S_2 = (1/2, 0, \sqrt{3}/2)$.

Given the initial position and the initial spins, these equations can be solved numerically for the initial values of P_θ and P_ϕ, thereby giving a complete set of initial conditions.

When the spin-spin terms are included, we can always initially satisfy the conditions for quasicircularity [Eqs. (3.5), (3.6), and (3.7)], but these conditions are not preserved by the evolution, since in this case orbits with constant radial separation no longer exist; the radial position oscillates as a function of time. These spin-induced radial oscillations can have non-negligible amplitudes at small separations, and it is unclear whether they represent orbits that could result from the adiabatic inspiral of quasicircular orbits under radiation reaction. A better method would be to set quasicircular initial conditions when the black holes are rather far apart (so that spin effects are negligible) and then evolve the system toward the final plunge by including radiation reaction in the dynamics. The calculation of radiation reaction effects for the Hamiltonian framework with spin couplings is currently under completion [18]; we plan to include them in the dynamics and investigate chaotic behaviors in the near future.

C. Post-Newtonian orbits at various orders

Here we show some of the effects of turning on or off the various post-Newtonian terms. We use quasicircular orbits to make the effects especially easy to see, but this is not a necessary restriction. Figures 1 and 2 show that the PN equations capture the essential aspects of relativistic orbits, such as the characteristic precession of the orbital plane.

Figures 3–5 show quasicircular orbits satisfying Eqs. (3.4), (3.5), (3.6), and (3.7), with increasing orders (up to 2PN) of the PN Hamiltonian included. The third

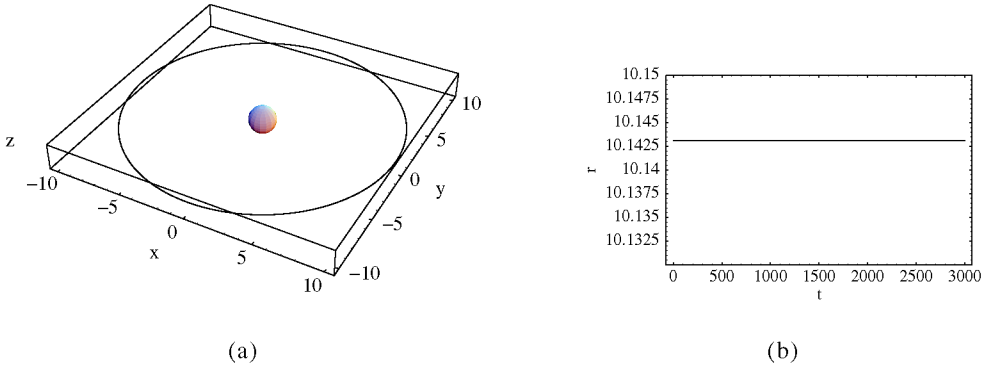

(a) (b)

FIG. 3 (color online). A post-Newtonian quasicircular orbit of two maximally spinning $10M_\odot$ black holes, with Newtonian, 1PN, and 2PN terms turned on. (a) The orbit embedded in Euclidean space; (b) the radius $r = \sqrt{x^2 + y^2 + z^2}$ as a function of time. Lengths are measured in terms of the total mass $M = m_1 + m_2$, and we show a schematic horizon at $r_H = M$.

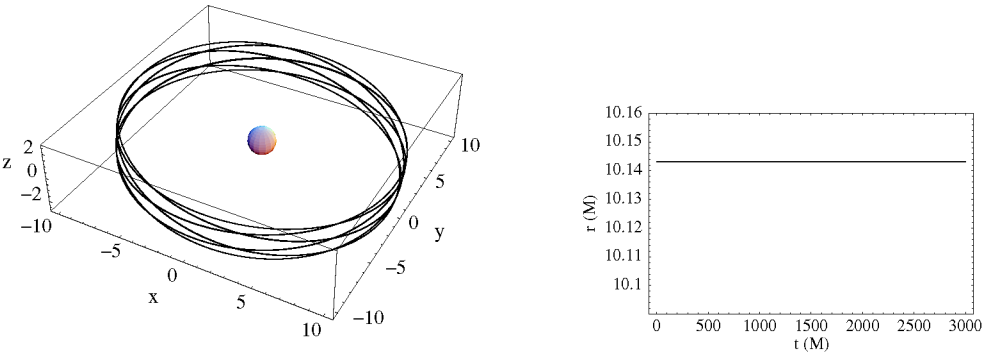

(a) (b)

FIG. 4 (color online). A post-Newtonian quasicircular orbit of two maximally spinning $10M_\odot$ black holes, with terms through spin-orbit coupling. (a) The orbit embedded in Euclidean space; (b) the radius $r = \sqrt{x^2 + y^2 + z^2}$ as a function of time. Lengths are measured in terms of the total mass $M = m_1 + m_2$, and we show a schematic horizon at $r_H = M$. The addition of spin-orbit coupling to the N, 1PN, and 2PN terms destroys exact circularity, but exact sphericity is preserved.

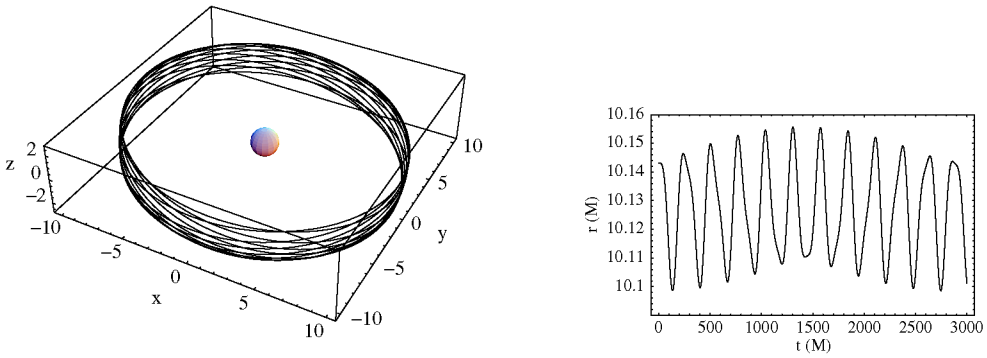

(a) (b)

FIG. 5 (color online). A post-Newtonian quasicircular orbit of two maximally spinning $10M_\odot$ black holes, with all the terms from Sec. II A (including all the spin-spin couplings) present. (a) The orbit embedded in Euclidean space; (b) the radius $r = \sqrt{x^2 + y^2 + z^2}$ as a function of time. Lengths are measured in terms of the total mass $M = m_1 + m_2$, and we show a schematic horizon at $r_H = M$. The addition of spin-spin coupling to the N, 1PN, 2PN, and spin-orbit terms destroys exact sphericity, but Eqs. (3.4), (3.5), (3.6), and (3.7) are still satisfied, leading to nearly circular orbits for these initial conditions.

figure includes all the spin-spin terms (S_1S_2, S_1S_1, and S_2S_2); we do not show any orbits with subsets of these terms activated because, to the precision visible in the figure, the S_1S_2 term dominates, and the figure is identical with either of the other terms removed.

IV. INVESTIGATING CHAOS IN THE POST-NEWTONIAN EQUATIONS

Previous studies of chaos in the post-Newtonian equations considered comparable mass-ratio binaries with eccentric orbits [2,4,19–21]. Here, we also consider comparable mass-ratio binaries and focus first on quasicircular orbits and then on eccentric orbits. As noted in the introduction, these orbits are particularly important because many astrophysically relevant binary systems should circularize due to the energy lost to gravitational radiation. We set the radii of these orbits so that the frequencies of their corresponding gravitational waves lie in a range $40\ \text{Hz} < f_{\text{GW}} < 240\ \text{Hz}$, roughly corresponding to the frequency band for the Laser Interferometer Gravitational-Wave Observatory (LIGO) and VIRGO. [More properly, we choose radii such that the *Newtonian* frequency of the gravitational waves (which is simply twice the orbital frequency) lies in the LIGO/VIRGO band, as discussed in Sec. IV B below.] For initial separations such that the Newtonian GW frequency is smaller than 40 Hz, we never find chaotic quasicircular orbits.

A. A brief discussion of Lyapunov exponents

As in previous works [5,6], Lyapunov exponents are our primary tool for investigating the nonlinear dynamics of general relativistic systems. We have discussed at length in [5,16] our techniques for calculating these exponents for systems similar to the PN equations. Here we present a brief summary of Lyapunov exponents.

Given an initial condition in the phase space of a dynamical system with n degrees of freedom, we imagine an n-dimensional ball of nearby initial conditions centered on that point. As the dynamics unfold, in general the ball is stretched in some directions and squeezed in others, deforming into an n-dimensional ellipsoid under the action of the flow. Such an ellipsoid has n principal (semi)axes, and the average rate of stretching or squeezing of each axis is a *Lyapunov number*, whose natural logarithm is the *Lyapunov exponent* associated with the axis. In general, the ith Lyapunov exponent of a dynamical system is

$$\lambda_i = \lim_{t\to\infty} \frac{\log[r_i(t)]}{t}, \tag{4.1}$$

where $r_i(t)$ is the ith principal ellipsoid axis. Implementing this prescription numerically leads to a visualization of the exponents as a plot of $\log[r_i(t)]$ vs t (so that the slope is the exponent λ_i), which we refer to as a *Lyapunov plot*. The result for a chaotic PN orbit appears in Figs. 6 and 7.

In practice, following the evolution of the phase-space ellipsoid, and thereby extracting all the Lyapunov exponents of the system, involves using the Jacobian matrix of the system to model an "infinitesimal" ball that captures the true linear approximation to the dynamics. It is also possible, and computationally faster, to extract only the largest Lyapunov exponent by considering only one nearby initial condition, joined by some small deviation vector to the original point. In what follows, most of our simulations use this faster (but less robust) *deviation vector* method, but we have checked many of the results using the Jacobian method. Further details of the various techniques for calculating Lyapunov exponents appear in [5] and especially [16].

It is worth noting that we can think of the PN system as *constrained*, since we wish to think of the spin magnitudes as fixed. In other words, given an initial spin vector, a

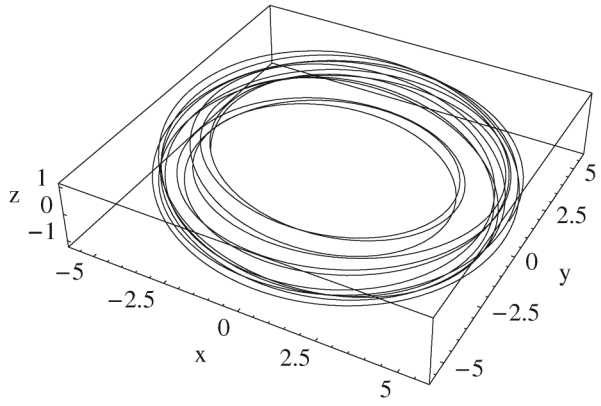

FIG. 6. The orbit of two maximally spinning $10M_\odot$ black holes. The dynamics are chaotic, as shown in Fig. 7. The initial conditions satisfy the requirements for quasicircularity, though in fact the orbit's radius is not even approximately constant (see Sec. IV B 3 below). The initial radius is $5.658M$, corresponding to an orbit with a Newtonian gravitational-wave frequency of $f_{\rm GW} = 240$ Hz [Eq. (4.4)]. The initial spins are $\mathbf{S}_1 = (0.130\,36, 0.262\,852, -0.955\,989)m_1^2$ and $\mathbf{S}_2 = (0.118\,966, -0.134\,59, -0.983\,734)m_2^2$. The other initial conditions are fixed by the conditions for quasicircularity (Sec. III B).

''nearby'' initial spin should point in a different direction but have the same magnitude. The system thus has only ten true degrees of freedom (three for relative position and momentum, and two for each spin), and should therefore have only ten Lyapunov exponents. The constraints lead to significant complications in calculating the Lyapunov exponents; see [16] for several methods of addressing these complications.

The principal value of the largest Lyapunov exponent is that it provides the e-folding time scale $t_\lambda = 1/\lambda$ for the divergence of nearby trajectories. The formal definition of λ in Eq. (4.1) requires an infinite-time limit, but of course any numerical method for λ must introduce some finite cutoff. As a result, in general it is impossible to say with any certainty that a system is not chaotic—even if it appears that $\lambda_{\rm max} \to 0$ for some $t_{\rm cutoff}$, chaos may yet manifest itself on longer time scales. Nevertheless, it is possible to calculate nonchaotic *baseline orbits* (corresponding, for example, to the PN terms through the spin-orbit coupling), whose nearby initial conditions still exhibit some nonzero (power-law) separation. If a suspected chaotic orbit has a Lyapunov exponent with a magnitude similar to a baseline orbit, we say that it is indistinguishable from or consistent with zero, and hence is probably not chaotic.

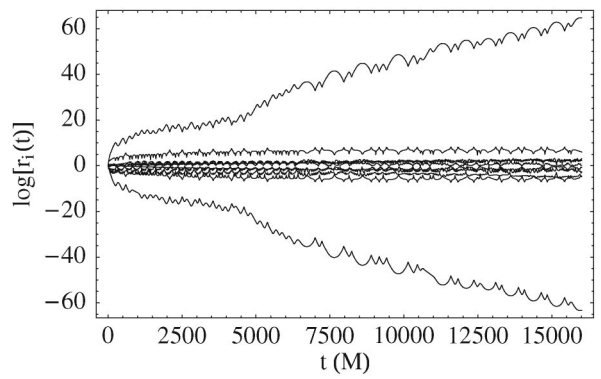

FIG. 7. The natural logarithms of the ellipsoid axes r_i vs t for the system shown in Fig. 6. The slopes of the lines are the Lyapunov exponents. Two nonzero exponents are clearly visible ($\lambda = \pm 3.2 \times 10^{-3} M^{-1}$), but all the others are consistent with zero. The curve with the largest slope corresponds to the upper line in Fig. 8. There is an apparent $\pm\lambda$ symmetry: for each exponent $+\lambda$, there is a corresponding exponent $-\lambda$; even the zero exponents approach zero symmetrically. This behavior is a characteristic of Hamiltonian systems [35].

For the present problem, the most relevant time scale is the inspiral time due to the energy loss from gravitational radiation. For the quasicircular orbits considered below, this is approximately given by the following formula [22],

$$t_{\rm insp} = \frac{5}{256}\frac{M^2}{\mu}\left(\frac{r}{M}\right)^4, \tag{4.2}$$

where M is the total mass and μ is the reduced mass. For eccentric orbits we use Eq. (5.14) of [22]. We then adopt the criterion $t_\lambda < t_{\rm insp}$ as an operational definition of chaos, which is equivalent to the condition

$$\lambda t_{\rm insp} > 1 \qquad \text{condition for chaotic orbit.} \tag{4.3}$$

On the other hand, if $t_\lambda > t_{\rm insp}$, then, even if the system is formally chaotic in the conservative limit we consider here, the chaos will not have time to manifest itself before the final plunge.

B. A survey of quasicircular orbits

In this section, we elucidate the effects of varying the parameters in the PN equations of motion on the presence of chaos in the resulting dynamics. In many of the examples, we parametrize the orbits by their radii, or, equivalently, by the ''gravitational-wave frequency'':

$$f_{\rm GW}^{\rm Newt} = \frac{1}{\pi}\left(\frac{GM}{r^3}\right)^{1/2}, \tag{4.4}$$

where we restore the factor of G so that the result is in Hz. It is essential to note that Eq. (4.4) is the *Newtonian* gravitational-wave frequency, which is valid only for radii that satisfy $r \gg M$. Nevertheless, Eq. (4.4) provides a convenient way to parametrize the initial conditions by radius in a way that has transparent physical significance in the nonrelativistic limit. When we refer below to an orbit with gravitational-wave frequency of (say) 240 Hz, we mean an orbit with a radius that satisfies Eq. (4.4) when $f_{\rm GW}^{\rm Newt} = 240$ Hz. It is important to remember that this is not in general the true frequency of the gravitational wave—for example, at 2PN order, for equatorial orbits,

averaging over an orbit yields [8,23,24]

$$f_{\rm GW}^{\rm 2PN} = \frac{1}{\pi}\left(\frac{GM}{r^3}\right)^{1/2}\Bigg\{1 + \frac{1}{2}(-3+\eta)\frac{GM}{r} - \frac{1}{2}\frac{1}{M^2}\hat{\mathbf{L}}\cdot\mathbf{S}_{\rm eff}\left(\frac{GM}{r}\right)^{3/2} + \frac{1}{2}\left(3 + \frac{7}{8}\eta + \frac{3}{4}\eta^2\right) \times \left(\frac{GM}{r}\right)^2 + -\frac{3}{4}\frac{1}{\eta}\frac{1}{M^4}[(\mathbf{S}_1\cdot\mathbf{S}_2) - 3(\hat{\mathbf{L}}\cdot\mathbf{S}_1)(\hat{\mathbf{L}}\cdot\mathbf{S}_2)]\left(\frac{GM}{r}\right)^2\Bigg\} \quad (4.5)$$

with $\hat{\mathbf{L}} = \mathbf{L}/|\mathbf{L}|$. For a binary with total mass $(10+10)M_\odot$ at radius $r = 5.5658M$ ($f_{\rm GW}^{\rm Newt} = 240$ Hz), Eq. (4.5) gives $f_{\rm GW}^{\rm 2PN} = \{181, 194, 212\}$ Hz when spins are aligned with (orbital) angular momentum, zero, and anti-aligned with angular momentum, respectively. For the same spin orientations at $r = 5.742M$ ($f_{\rm GW}^{\rm Newt} = 150$ Hz), Eq. (4.5) gives $f_{\rm GW}^{\rm 2PN} = \{122, 127, 134\}$ Hz.

1. A chaotic quasicircular orbit

We find that post-Newtonian orbits satisfying the conditions for quasi circularity (Sec. III B) can be chaotic (though *only* for rather small initial radial separations), as shown in Figs. 6–8. Note from Fig. 7 that the Lyapunov exponents come in $\pm\lambda$ pairs, a characteristic of Hamiltonian dynamical systems. Note also that the principal exponent calculated using the deviation vector method (Fig. 8) agrees closely with the largest exponent determined from Fig. 7, which uses the more complicated Jacobian method to find the exponents.

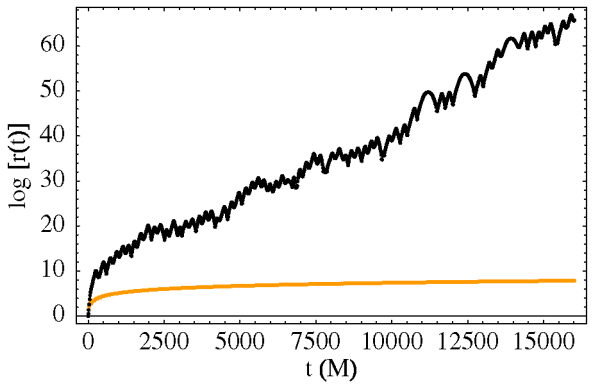

FIG. 8 (color online). The natural logarithm of the principal ellipsoid axis vs time for the system shown in Fig. 6, using the deviation vector method. The slope of the line is the Lyapunov exponent, which is approximately $\lambda = 3.2\times10^{-3}M^{-1}$ using a least-squares fit (which agrees closely with the value from Fig. 7, which uses the more sophisticated Jacobian method to find the exponent). This corresponds to a Lyapunov (e-folding) time scale of $t_\lambda = 1/\lambda = 3.1\times10^2 M$, which is less than a fifth of the inspiral time scale. The simulation data for a nonchaotic orbit (light) is shown for reference.

2. Varying spin directions

We illustrate the effect of varying the spin directions by generating a large number of quasicircular orbits with randomly oriented (maximal) spins. For each spin configuration, we choose the radius corresponding to a gravitational wave with frequency $f_{\rm GW}^{\rm Newt} = 240$ Hz (the high end of the LIGO/VIRGO frequency band). The choice of radius is motivated by two main factors. First, choosing the lowest possible radius (consistent with the abilities to detect the corresponding gravitational waves) likely represents a worst-case scenario for chaos, since low-radius regions correspond to stronger nonlinearities in the equations of motion (as noted in [6]). Second, minimizing the radius minimizes the inspiral time scale $t_{\rm insp}$, which in turn minimizes the computational cost of a final integration time significantly longer than $t_{\rm insp}$. This allows us to achieve a better bound on the suspected zero Lyapunov exponent, and increases our confidence that apparent nonzero exponents represent genuine chaotic behavior. In what follows, the final integration time is 10 times the inspiral time of each orbit.

We consider the following mass configurations: $(20+5)M_\odot$, $(10+5)M_\odot$, $(5+5)M_\odot$, $(10+10)M_\odot$, $(20+20)M_\odot$, $(20+10)M_\odot$, and $(15+5)M_\odot$. The result of choosing $N = 500$ randomly oriented initial spins for each case appears in Table I. We find the presence of chaotic orbits for the $(10+10)M_\odot$ and $(20+10)M_\odot$ cases, but we find no chaos for any other configuration. Figure 8 shows a Lyapunov plot for the strongest chaos in our simulation data. The onset of chaos is marked by a

TABLE I. The prevalence of chaos in post-Newtonian quasicircular orbits at 240 Hz, for spin directions chosen randomly on a unit sphere. We calculate the fraction of orbits whose e-folding times $t_\lambda = 1/\lambda$ are less than the inspiral time $t_{\rm insp}$, which is our operational definition of chaos. The final integration time is 10 times the inspiral time. We also include 95% confidence intervals for the reported fractions, and we show the average value of λ measured in units of the inverse inspiral time for the $(20+10)M_\odot$ configuration (the only case in our simulation with more than one chaotic orbit). The simulation data represent 500 randomly chosen initial spin directions for each configuration, with the initial radius fixed by requiring a gravitational-wave frequency of 240 Hz (as determined by the Newtonian formula).

Configuration	Fraction chaotic	95% confidence interval	Average chaotic $\lambda t_{\rm insp}$
$(20+5)M_\odot$	0	[0, 0.007 38]	
$(10+5)M_\odot$	0	[0, 0.007 38]	
$(5+5)M_\odot$	0	[0, 0.007 38]	
$(10+10)M_\odot$	0.002	$[5.06\times10^{-5}, 0.0111]$	
$(20+20)M_\odot$	0	[0, 0.007 38]	
$(20+10)M_\odot$	0.104	[0.0777, 0.136]	1.45
$(15+5)M_\odot$	0	[0, 0.007 38]	

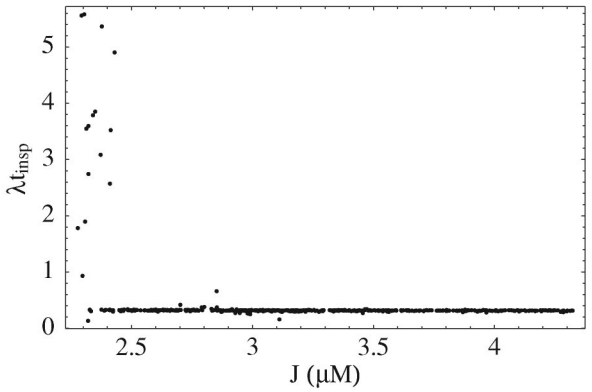

FIG. 9. Lyapunov exponents for 500 quasicircular orbits as a function of total angular momentum J for the $(10 + 10)M_\odot$ configuration. The spin for each body is maximal with random initial spin angles (θ, ϕ) (which overweights the poles). The initial radius corresponds to a gravitational-wave frequency of $f_{\rm GW}^{\rm Newt} = 240$ Hz. The Lyapunov exponents are measured in terms of the inverse inspiral time $1/t_{\rm insp}$, so that $\lambda t_{\rm insp} > 1$ indicates that nearby trajectories diverge by a factor of e on a time scale shorter than the inspiral time scale. There are 14 such chaotic initial conditions out of the 500 orbits considered for this configuration. They are clustered at the low end of the angular momentum range, indicating that the spins are closely aligned with each other and anti-aligned with the orbital angular momentum.

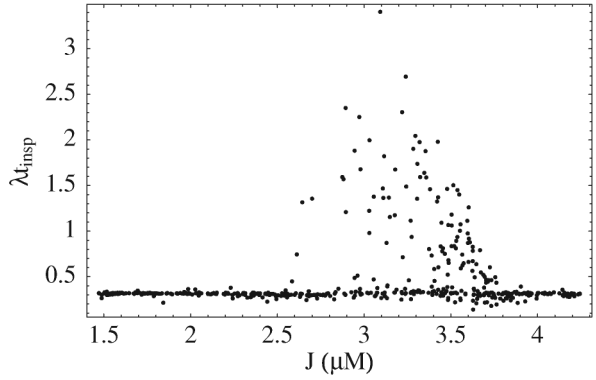

FIG. 10. Lyapunov exponents for 500 quasicircular orbits as a function of total angular momentum J for the $(20 + 10)M_\odot$ configuration. The spin for each body is maximal and randomly oriented, and the initial radius corresponds to a gravitational-wave frequency of $f_{\rm GW}^{\rm Newt} = 240$ Hz. The Lyapunov exponents are measured in terms of the inverse inspiral time $1/t_{\rm insp}$, so that $\lambda t_{\rm insp} > 1$ indicates that nearby trajectories diverge by a factor of e on a time scale shorter than the inspiral time scale. There are 49 such chaotic initial conditions out of the 500 orbits considered for this configuration. Unlike the $(10 + 10)M_\odot$ case shown in Fig. 9, the chaotic orbits in this case correspond to total angular momentum in the middle of the range.

transition from linear (or at most power-law) separation of nearby initial conditions to exponential separation. On our Lyapunov plot (which is logarithmic on its vertical axis), chaotic orbits appear as linear growth.

Our initial simulation for the $(10 + 10)M_\odot$ configuration used random spin angles (θ, ϕ), which does not correspond to a random orientation but rather overweights the poles. This was a stroke of good luck: as shown in Fig. 9, for $(10 + 10)M_\odot$ the chaotic orbits are clustered at the lowest values of the total angular momentum J, corresponding to initial spin vectors nearly anti-aligned with the orbital angular momentum $\mathbf{L}$ (so that $J = |\mathbf{L} + \mathbf{S}|$ is minimized). When running the simulation again using randomly oriented spins, we find only one chaotic orbit for this configuration. The association of chaos with low values of $\mathbf{J}$ holds also for the sole chaotic orbit found in the $(10 + 5)M_\odot$ case, but it is not a general result: as Fig. 10 shows, chaos for the $(20 + 10)M_\odot$ configuration occurs mainly for values of J in the middle of the possible range.

3. Varying initial frequencies

We now investigate the results of varying the initial (gravitational-wave) frequencies for the strongest chaotic orbit from the previous section (as illustrated in Fig. 8). The result appears in Fig. 11, which shows that, even for this worst-case scenario, i.e., the system with the largest Lyapunov exponent, chaos is absent for initial radii corresponding to $f_{\rm GW}^{\rm Newt}$ less than 160 Hz. Above 160 Hz, there is an abrupt change in the dynamics from regular to chaotic (Fig. 12), with a maximum Lyapunov exponent more than 18 times the inverse inspiral time (meaning that nearby trajectories diverge by a factor of e in a time $t_\lambda \approx t_{\rm insp}/18$).

Cornish and Levin have recently pointed out [25] that if unstable orbits are perturbed they could become locus of chaos. The abrupt transition from nonchaotic to chaotic behavior that we observe in Fig. 11, when we increase the GW frequency (and hence lower the radial separation), could correspond to the transition from stable to unstable

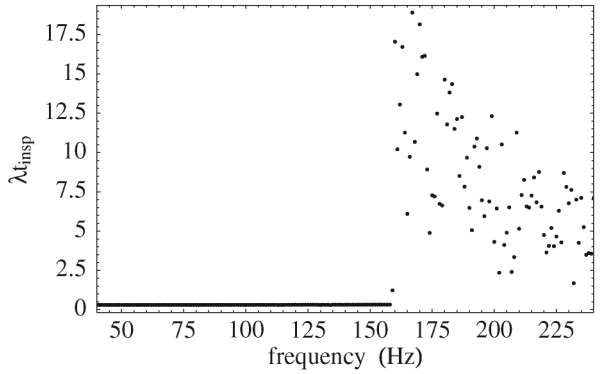

FIG. 11. Lyapunov exponents as a function of the (Newtonian) gravitational-wave frequency for quasicircular orbits of two maximally spinning $10M_\odot$ black holes. The Lyapunov exponents are measured in terms of the inverse inspiral time $1/t_{\rm insp}$, and the frequencies are chosen to correspond closely to the LIGO/VIRGO frequency band. There is an abrupt transition to chaos at approximately 160 Hz.

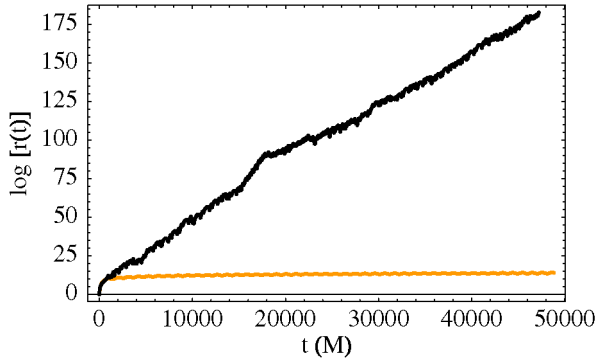

FIG. 12 (color online). The natural logarithms of the principal ellipsoid axes vs time for frequencies on opposite sides of the transition to chaos shown in Fig. 11: $f_{\rm GW}^{\rm Newt} = 158$ Hz (light) and $f_{\rm GW}^{\rm Newt} = 160$ Hz (dark). The slope of each line is the Lyapunov exponent, with $\lambda \approx 7 \times 10^{-5} M^{-1}$ (light, nonchaotic/consistent with zero) and $\lambda \approx 4 \times 10^{-3} M^{-1}$ (dark, chaotic). The orbits corresponding to these two frequencies appear in Figs. 13 and 14.

orbits in the spinning ADM Hamiltonian. Thus, to better understand the onset of chaos, it would be worthwhile to explore this intuition further by applying some stability criterion in the Hamiltonian framework of the kind worked out in the nonspinning case by [24].

In this particular case, the qualitative change in the dynamical behavior from nonchaotic to chaotic is mirrored in the orbits themselves. In particular, the onset of chaos is associated with a breakdown in the quasicircularity of the orbit. As shown in Fig. 13, just below the transition to chaos the orbit is nearly circular. Just above the transition, despite satisfying the conditions for quasicircularity at initial time, the orbits are not even approximately circular

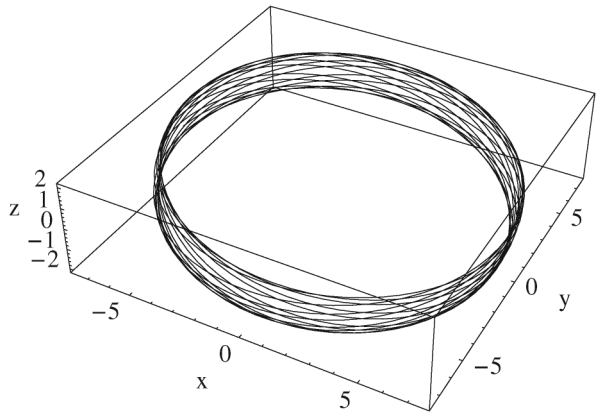

FIG. 13. The nonchaotic quasicircular orbit of two maximally spinning $10M_\odot$ black holes, corresponding to a gravitational-wave frequency of $f_{\rm GW}^{\rm Newt} = 158$ Hz. The spins are the same as in Fig. 6. The corresponding Lyapunov plot is shown in Fig. 12. The orbit's radius is approximately constant, as required for a true quasicircular orbit.

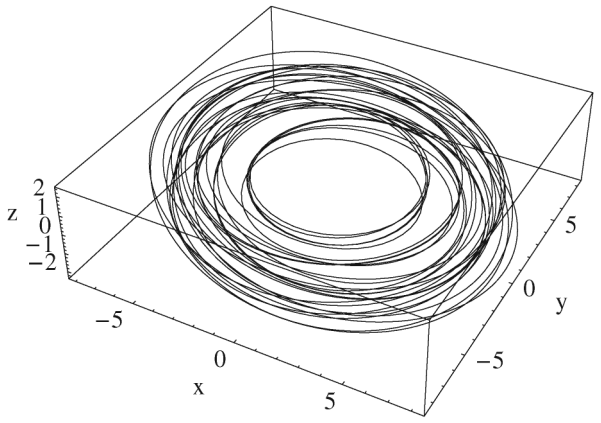

FIG. 14. The chaotic quasicircular orbit of two maximally spinning $10M_\odot$ black holes, corresponding to a gravitational-wave frequency of $f_{\rm GW}^{\rm Newt} = 160$ Hz. The spins are the same as in Fig. 6. The corresponding Lyapunov plot is shown in Fig. 12. Note that the quasicircularity has broken down; the radius is not even approximately constant. This qualitative change in the orbit accompanies the onset of chaos as the frequency increases (with a corresponding decrease in radius), as illustrated in Fig. 11.

along the evolution because of the strong spin coupling, as shown in Fig. 14.

To verify that the disappearance of chaos at lower frequencies is generic, we repeated the 240 Hz survey for the lower end of the frequency range considered ($f_{\rm GW}^{\rm Newt} =$ 40 Hz). The inspiral times are very long in this case, requiring patience on the part of the simulator, but the results are gratifying: as shown in Table II, we found not even one orbit with a Lyapunov time less than the inspiral time at 40 Hz. Any chaos, if present, manifests itself in this case on time scales longer than $t_{\rm insp}$.

TABLE II. The prevalence of chaos in post-Newtonian quasicircular orbits at 40 Hz, for spin directions chosen randomly on a unit sphere. We calculate the fraction of orbits whose e-folding times $t_\lambda = 1/\lambda$ are less than the inspiral time $t_{\rm insp}$, which is our operational definition of chaos. The final integration time is 10 times the inspiral time. We also include 95% confidence intervals for the reported fractions. The simulation data represent 500 randomly chosen initial spin directions for each configuration, with the initial radius fixed by requiring a gravitational-wave frequency of 40 Hz (as determined by the Newtonian formula). In this case, the number of chaotic orbits for each configuration is zero.

Configuration	Fraction chaotic	95% confidence interval
$(20 + 5)M_\odot$	0	[0, 0.007 38]
$(10 + 5)M_\odot$	0	[0, 0.007 38]
$(5 + 5)M_\odot$	0	[0, 0.007 38]
$(10 + 10)M_\odot$	0	[0, 0.007 38]
$(20 + 20)M_\odot$	0	[0, 0.007 38]
$(20 + 10)M_\odot$	0	[0, 0.007 38]
$(15 + 5)M_\odot$	0	[0, 0.007 38]

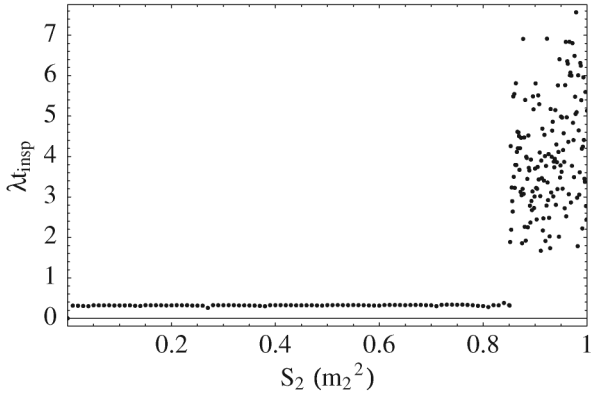

FIG. 15. Lyapunov exponents as a function of spin for quasicircular orbits of two $10M_\odot$ black holes. We fix the spin of one hole at the maximum value ($S_1 = m_1^2$), and also fix the spin directions (which are the same as in Fig. 6), and then vary the spin S_2 of the second body. The Lyapunov exponents are measured in terms of the inverse inspiral time $1/t_{\rm insp}$. There is an abrupt transition to chaos when S_2 exceeds 0.85 (measured in units of m_2^2).

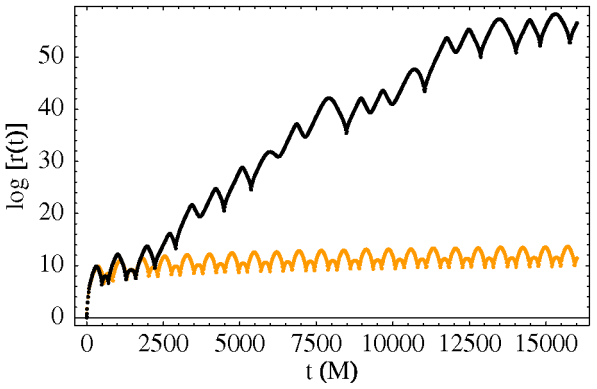

FIG. 16 (color online). The natural logarithms of the principal ellipsoid axes vs time for values of S_2 on opposite sides of the transition to chaos shown in Fig. 15: $S_2 = 0.83$ (light) and $S_2 = 0.86$ (dark). The slope of each line is the Lyapunov exponent, with $\lambda \approx 2.0 \times 10^{-4} M^{-1}$ (light, nonchaotic/consistent with zero) and $\lambda \approx 3.5 \times 10^{-3} M^{-1}$ (dark, chaotic). The orbits corresponding to these two spins appear in Figs. 17 and 18.

4. Varying spin magnitudes

In Sec. IV B 3, we created a one-parameter family of orbits by taking the worst offender from Sec. IV B 2 and varying the frequency (or, equivalently, the quasicircular radius). In this section, we do the same, but fix the frequency and vary the magnitude of one of the spins.

We showed in Sec. IV B 2 that the worst-offender orbit (with $m_1 = m_2 = 10M_\odot$) is chaotic when $S_2 = 1$ (measured in units of m_2^2). As shown in Fig. 15, the dynamics are nonchaotic for most values of S_2, with a transition to chaos at approximately $S = 0.85$. Since the dynamics are nonchaotic when $S_2 = 0$, the chaos must be produced by the spin terms in the Hamiltonian.

In Fig. 16, we show Lyapunov plots for orbits on either side of the chaotic transition. Although the difference is not as dramatic as the frequency-induced transition (Fig. 12), there is still a qualitative change in the value of the principal Lyapunov exponent. Unlike the system in Sec. IV B 2, this transition does not give rise to a qualitative change in the orbit as the spin is varied. Instead, the chaos manifests itself in the time evolution of the spins, as shown in Figs. 17 and 18.

5. Varying the PN terms

The previous results in this section included all the PN terms described in Sec. II A, with the exception of the 3PN term. Here we investigate the effect of varying these terms. We first consider the effect of the 3PN term, and then investigate the effects of turning off one or more of the spin terms.

In order to evaluate the effect of the 3PN term on chaos in the post-Newtonian equations, we recalculate the simulation of 500 orbits in the $(20 + 10)M_\odot$ system shown in Fig. 10; the result appears in Fig. 19. There are some minor differences, including a slight suppression of the most chaotic orbit, but the effect of 3PN is not strong. This result holds also for the $(10 + 10)M_\odot$; in this case we examine the transition to chaos shown in Fig. 11. As seen in Fig. 20, the transition occurs at a slightly lower frequency, but the difference between the two cases is

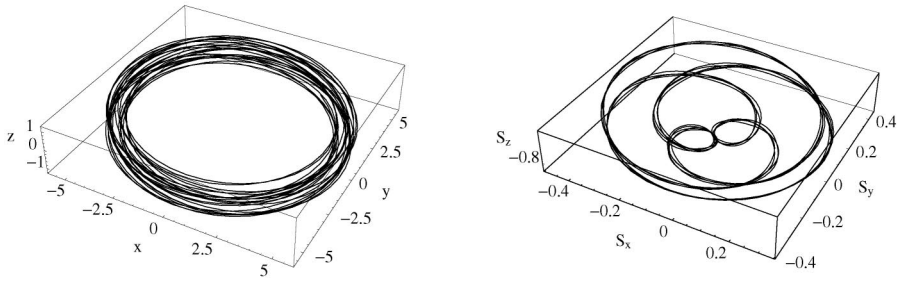

(a) (b)

FIG. 17. (a) The nonchaotic quasicircular orbit of two $10M_\odot$ black holes, with spin magnitudes of $S_1 = 1$ and $S_2 = 0.83$; (b) Cartesian "spin space" showing the time evolution of S_x, S_y, and S_z. Compare with Fig. 18(b). The corresponding Lyapunov plot is shown in Fig. 16.

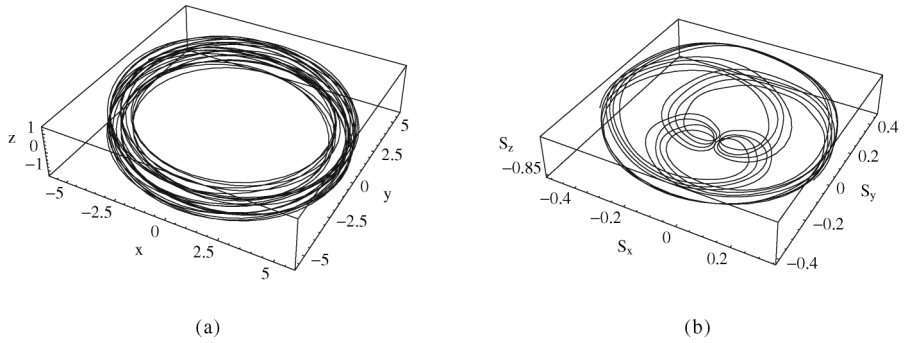

FIG. 18. (a) The chaotic quasicircular orbit of two $10M_\odot$ black holes, with spin magnitudes of $S_1 = 1$ and $S_2 = 0.86$; (b) Cartesian "spin space" showing the time evolution of S_x, S_y, and S_z. The corresponding Lyapunov plot is shown in Fig. 16. There appears to be no qualitative difference between the orbit (a) and the orbit in Fig. 17(a), but there is a qualitative change in the spin behavior. Unlike the frequency transition shown in Fig. 12, which gives a qualitative change in the evolution of the spatial variables, the spin transition to chaos manifests primarily itself in the spin degrees of freedom.

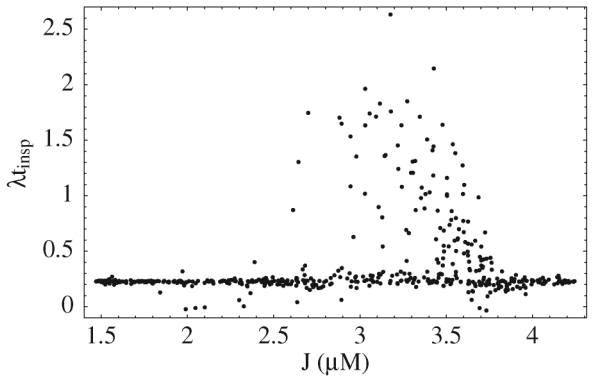

FIG. 19. Lyapunov exponents for 500 quasicircular orbits as a function of total angular momentum J for the $(20 + 10)M_\odot$ configuration with 3PN term added. The initial conditions are identical to those in Fig. 10; the prevalence of chaos is not strongly affected by the presence of the 3PN term.

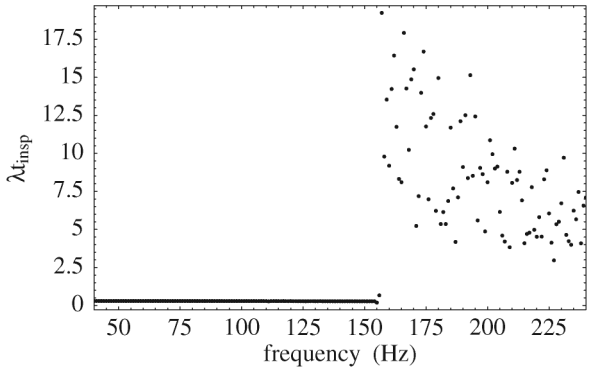

FIG. 20. Lyapunov exponents as a function of (Newtonian) gravitational-wave frequency for quasicircular orbits of two maximally spinning $10M_\odot$ black holes with 3PN term added. The Lyapunov exponents are measured in terms of the inverse inspiral time $1/t_{\rm insp}$, and the frequencies are chosen to correspond closely to the LIGO frequency band. There is an abrupt transition to chaos at approximately 155 Hz. The initial conditions are identical to those in Fig. 11.

small. Our general conclusion is that the third post-Newtonian term has only minor effects on the presence of chaos.

In order to investigate the effect of the spin terms in the post-Newtonian Hamiltonian, we focus first on the strongest chaos found in our simulations of the $(20 + 10)M_\odot$ configuration for $f_{\rm GW}^{\rm Newt} = 40$ Hz with 3PN turned on, as shown in Fig. 10. The Lyapunov plots for a variety of PN term combinations appears in Fig. 21. The most important result is that the spin-spin terms are crucial to the presence of chaos; when only Newtonian, 1PN, 2PN, 3PN and spin-orbit are turned on, the system is not chaotic. In the case illustrated in Fig. 21, the S_1S_2 term by itself causes chaos: the presence of either the spin quadrupole term is irrelevant. This is not a general result: Fig. 22 shows a case where the S_1S_1 quadrupole term apparently exerts a stabilizing influence: when only S_2S_2 is turned off, the system is nonchaotic, but if S_1S_1 is then turned off as well the system returns to chaotic behavior.

C. Eccentric orbits

Although quasicircular orbits represent the most likely source of gravitational waves from compact binaries detectable by ground-based observatories, some sources may consist of binaries with non-negligible eccentricity (such as produced, for example, by the Kozai mechanism [26,27]). It is therefore potentially relevant to investigate chaos for eccentric orbits.

1. A chaotic eccentric orbit

In agreement with [4,28], we find that the post-Newtonian equations can produce chaotic eccentric orbits; one example appears in Fig. 23. It must be emphasized that, as in the case of quasicircular orbits, the pericenter of the

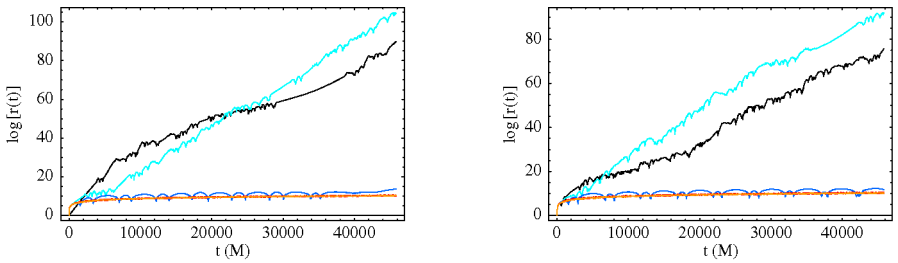

FIG. 21 (color online). The natural logarithms of the longest ellipsoid axis r vs t for the strongest chaos found in the $(20 + 10)M_\odot$ configuration (as illustrated in Fig. 10), for varying post-Newtonian terms: (a) 3PN turned off; (b) 3PN turned on. The final time is 50 times the inspiral time, and the slopes of the lines are the Lyapunov exponents. In all cases, the Newtonian, 1PN, 2PN, and spin-orbit terms are turned on, but some of the others may be turned off; from top to bottom (with colors, visible in electronic versions of this paper, noted parenthetically): all PN terms (black); S_1S_1 and S_2S_2 turned off (cyan); S_1S_1 turned off (blue, nonchaotic); S_2S_2 turned off (red, nonchaotic); S_1S_1, S_2S_2, and S_1S_2 turned off (orange, nonchaotic). For this particular case, the S_1S_2 spin-coupling term is necessary for chaos to appear.

orbit corresponding to Fig. 23 is at $r_p = 5M$; thus the two black holes are rather close to each other and higher order PN corrections, especially higher spin PN corrections, should also be taken into account. Nevertheless, it is clear that the equations themselves can produce chaotic solutions, even if those solutions have dubious physical relevance.

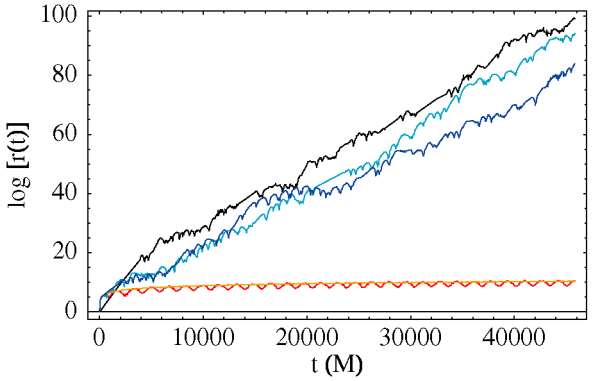

FIG. 22 (color online). The natural logarithms of the longest ellipsoid axis r vs t for a strongly chaotic $(20 + 10)M_\odot$ configuration, for varying post-Newtonian terms. The initial spins (both maximal) are $\mathbf{S}_1 = (-0.935\,125, 0.329\,567, 0.130\,101)m_1^2$ and $\mathbf{S}_2 = (0.039\,523, -0.543\,03, -0.838\,783)m_2^2$, while the initial radius is $r = 4.318M$, corresponding to $f_{\rm GW}^{\rm Newt} = 240$ Hz; the other initial conditions are fixed by the conditions for quasicircularity (Sec. III B). The final time is 50 times the inspiral time, and the slopes of the lines are the Lyapunov exponents. In all cases, the Newtonian, 1PN, 2PN, and spin-orbit terms are turned on, but some of the others may be turned off; from top to bottom (with colors, visible in electronic versions of this paper, noted parenthetically): all PN terms (black); S_1S_1 and S_2S_2 turned off (cyan); S_1S_1 turned off (blue); S_2S_2 turned off (wiggly/red, nonchaotic); S_1S_1, S_2S_2, and S_1S_2 turned off (straight/orange, nonchaotic).

2. Parameter variation

In order to give a sense of the relative importance of various orbital and spin parameters for the presence of chaos, we take the system shown in Fig. 23 and vary several parameters independently. In Fig. 24 we show the effect on the dimensionless Lyapunov exponent $\lambda t_{\rm insp}$ of varying the pericenter. Since the various spin terms (which make chaos possible) are decreasing functions of r, we might expect that the chaos is weaker or nonexistent as the spin terms get smaller, and indeed this is the case: for the model system we consider here, there is no chaos for $r_p > 6M$. Decreasing the eccentricity has a similar effect (Fig. 25); more highly eccentric orbits are more likely to be chaotic, probably because the larger velocities lead to

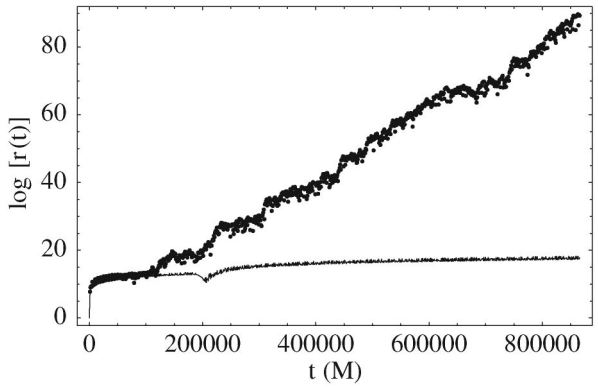

FIG. 23. The natural logarithms of the longest ellipsoid axis r vs t for a chaotic eccentric orbit. The slope of the line gives $\lambda t_{\rm insp} = 1.01$, so that nearby trajectories diverge by a factor of e in approximately one inspiral time. The initial conditions are $M_1 = 6$, $M_2 = 4$, $\mathbf{X} = (5, 0, 0)$, $\mathbf{P} = (0, 0.616\,44, 0.361\,60)$, $\mathbf{S}_1 = (-1.215\,70, -0.318\,59, 0.818\,86)$, and $\mathbf{S}_2 = (-0.152\,73, 0.645\,25, -0.069\,02)$. For reference, we show the corresponding plot for a nonchaotic orbit (with the same initial conditions as above except for $\mathbf{S}_1 = 0$).

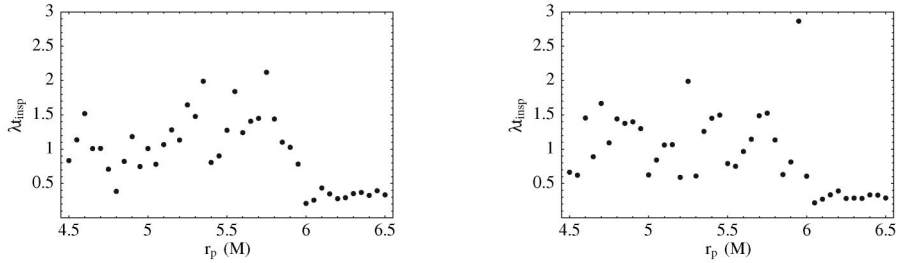

FIG. 24. The dimensionless Lyapunov exponent $\lambda t_{\rm insp}$ as a function of pericenter for (a) all terms through 2PN and (b) all terms through 3PN. The initial spins are the same as those in Fig. 23, with the other initial conditions fixed by the parametrization method described in Sec. III A. Note that the Lyapunov exponent decreases with increasing pericenter as the spin-coupling terms get smaller (consistent with the results in [5,6]).

larger values of the nonlinear velocity-dependent terms in the Hamiltonian. Finally, varying the value of the spin parameter for one of the bodies (Fig. 26) produces the expected result: as the spin decreases, the chaos is generally suppressed or disappears altogether. From Figs. 24–26, it is clear that adding the third post-Newtonian term has only minor effects in general on the presence of chaos.

3. A survey of eccentric orbits

We undertake here a survey of eccentric orbits in an effort to understand the prevalence of chaos in these systems. Unfortunately, in contrast to the quasicircular case (Sec. IV B), any survey of eccentric orbits is limited by the large number of parameters, which makes a comprehensive survey impractical. Nevertheless, we have examined thousands of initial conditions for a variety of masses and eccentricities, with special attention paid to systems that are realistic sources of gravitational radiation for ground-based detectors.

We consider binaries with masses of $(6+3)M_\odot$, $(6+4)M_\odot$, and $(12+3)M_\odot$. Our choices for the eccentricities and pericenters are then guided by astrophysical considerations [26,27]: eccentricities are not larger than ~ 0.33, and we choose the orbital frequency at pericenter such that the corresponding (Newtonian) gravitational-wave frequencies lie in the frequency band of ground-based interferometers (for low eccentricities GW radiation is emitted mostly at 1, 2, and 3 times the orbital frequency). The specific values we consider here, which satisfy the conditions above, are $e = 0.01, 0.2, 0.33$ and $f_{\rm orb} = 13.3, 20, 40, 50, 100$ Hz. [Note that at eccentricity ~ 0.22 (~ 0.33) the amplitudes of the Newtonian gravity-wave signal for the first and third harmonics are 17% (28%) and 40% (60%) relative to the second harmonic [29].] The pericenter is then obtained from the formula [30]

$$r_p = \frac{1-e}{(2\pi M f_{\rm orb})^{2/3}}. \tag{4.6}$$

With the choices made for e and $f_{\rm orb}$, Eq. (4.6) takes values between $8M$ and $30M$. Thus, the PN expansion is valid for the two compact bodies even at the point of closest approach.

For each value of the binary masses and for each pair (e, $f_{\rm orb}$) we produce 500 randomly oriented maximal initial spins and calculate the largest Lyapunov exponent as in

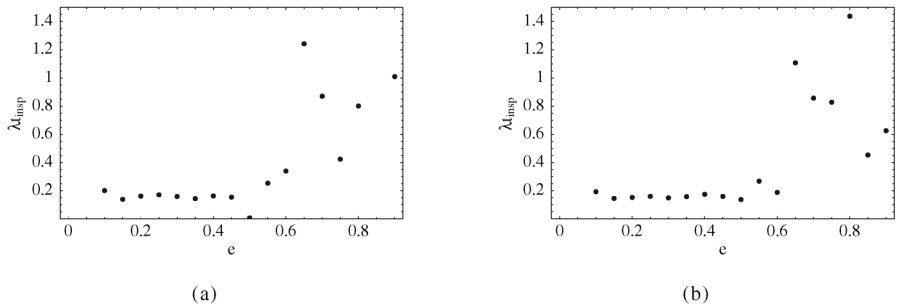

FIG. 25. The dimensionless Lyapunov exponent $\lambda t_{\rm insp}$ as a function of orbital eccentricity for (a) all terms through 2PN and (b) all terms through 3PN. Only eccentricities greater than around 0.6 show any evidence of chaos. The initial spins are the same as those in Fig. 23, with the other initial conditions fixed by the parametrization method described in Sec. III A.

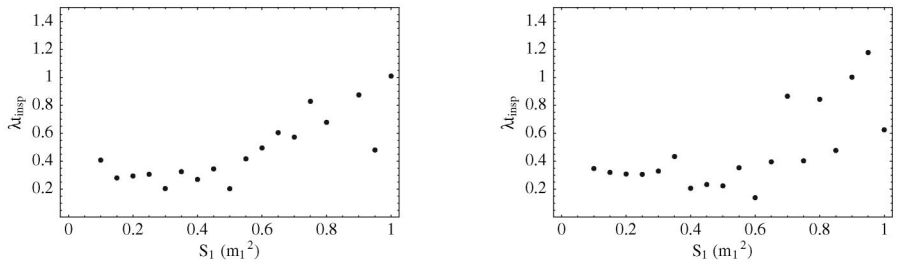

FIG. 26. The dimensionless Lyapunov exponent $\lambda t_{\rm insp}$ as a function of the first body's spin for (a) all terms through 2PN and (b) all terms through 3PN. The initial spins are the same as those in Fig. 23, with the other initial conditions fixed by the parametrization method described in Sec. III A. The strength of the chaos decreases as the spin decreases, becoming indistinguishable from zero below around $S_1 = 0.5m_1^2$.

Sec. IV B, using a final integration time of 10 times the inspiral time (as calculated from [22]). [For each random orientation we first fix the spin, and then use the method described in Sec. III A to find the initial conditions; in particular, the PN Hamiltonian in Eq. (3.3) always includes the spin contributions.] In all cases considered, we find no evidence of chaos—all the Lyapunov exponents are consistent with zero.

V. CONCLUSIONS

The dynamics of binary black holes, as modeled by the post-Newtonian equations, are significantly affected by the presence of spin. In particular, the addition of spin terms to the post-Newtonian equations of motion leads to significant changes in the orbital geometry and dynamical behavior of the solutions. The effects of the spin terms are particularly clear on quasicircular orbits, where the interaction terms quadratic in the spin cause deviations from perfectly spherical orbits.

We find that, for quasicircular orbits, the presence of the interaction terms quadratic in the spins can lead to chaotic solutions, as indicated by positive Lyapunov exponents. These exponents come in $\pm\lambda$ pairs, a reflection of the Hamiltonian nature of the dynamics. We measure the strength of the chaos by comparing the e-folding time scale for chaotic behavior (the inverse of the Lyapunov exponent) with the inspiral time scale. We find especially strong chaos for high-frequency/low-radius orbits and high spins. However, in those cases the black holes are so close to each other that spin-spin induced oscillations in the radial separation are rather important, and the quasicircular initial conditions used in this paper may not correspond to widely separated quasicircular orbits evolved adiabatically to low separations under gravitational radiation reaction. It would therefore be preferable to set initial conditions when the black holes are rather far apart (so that spin effects are negligible) and then evolve the system including radiation-reaction effects. The latter will be soon available [18] in the Hamiltonian framework, including spin couplings, and we plan to include them and investigate the presence of chaos in the near future.

We build a survey of eccentric orbits which we believe is representative of binaries which can emit GWs in the LIGO/VIRGO frequency band, have eccentricities justified by astrophysical considerations, and whose dynamics can be safely described by the PN expansion. For this survey we do not find any chaos. We find chaotic solutions only for rather eccentric orbits ($e \sim 0.9$) with very low pericenters, which are not astrophysically motivated and for which higher order PN terms, especially higher order spin couplings, should be consistently added in the ADM Hamiltonian.

Since we find that chaotic behavior is due to spin-spin couplings and does not seem to be much affected by the nonspinning PN dynamics, we suspect that our results will not change qualitatively if the nonspinning ADM Hamiltonian were replaced by the Schwarzschild deformed effective-one-body Hamiltonian [31,32] (which is a resummation of the ADM Hamiltonian). By contrast, we might expect differences if the Kerr-deformed effective-one-body Hamiltonian [15] were used instead of the spinning ADM Hamiltonian.

In conclusion, considering our surveys of quasicircular and eccentric orbits together, we find no chaos in any system for orbits that are of astrophysical interest for ground-based interferometers and which clearly satisfy the approximations required for the equations of motion to be physically valid at the post-Newtonian order considered.

ACKNOWLEDGMENTS

We wish to thank Yanbei Chen, Thibault Damour, and Sterl Phinney for useful interactions and Achamveedu Gopakumar for stimulating comments. M. D. H. acknowledges the support of NASA Grant No. NAG5-10707.

APPENDIX: NUMERICAL IMPLEMENTATION

Our primary implementation of the post-Newtonian equations of motion is a collection of *Mathematica* packages, relying on the native NDSOLVE function to effect numerical integrations. We implement the equations in a standard way to eliminate the mass variables, measuring lengths and times in terms of the total mass M and momenta in terms of the reduced mass μ. In these units, consistency then forces the angular momenta to be measured in terms of μM.

We perform various tests to check the validity of the equations of motion and the numerical integrations. Most important, we check that the energy, angular momentum, and spin magnitudes are all conserved by the integrations. These quantities are useful since they tend to be sensitive to mistakes in the equations of motion; we verify in all cases that the constants of the motion are conserved at a level consistent with the default accuracy goal (typically 10^{-10}), which gives us confidence that the equations are correct. We also check that orbital angular momentum and $\mathbf{L}\cdot\mathbf{S}_{\rm eff}$ are conserved through spin-orbit coupling, as discussed in Sec. II B. Furthermore, we verify that our implementation of the equations reproduces the Keplerian orbits of Newtonian gravitation (only Newtonian terms turned on), Lense-Thirring precession (extreme mass-ratio $m_1 \gg m_2$ limit with Newtonian and SO terms turned on), and classical quadrupole precession (Newtonian and S_1S_2 turned on).

A second implementation of the equations of motion uses a *Mathematica* interface for a C++ numerical integrator. We use *Mathematica* to generate the required derivative expressions directly from the Hamiltonian, using the built-in CFORM function to convert to C++ source code, so that the native *Mathematica* and C++ integrators automatically agree.[4] As in the case of the pure *Mathematica* integrator, we check the conservation of all the relevant quantities, in this case using a Bulirsch-Stoer integrator with an error goal of 10^{-10} (the variable EPS from Numerical Recipes [34]). We also check several orbits with a Runge-Kutta integrator with an error goal of 10^{-9}; the resulting agreement with the Bulirsch-Stoer integrations verifies that our results are not specific to the choice of integration algorithm.

As noted in Sec. IV A, for the calculation of Lyapunov exponents we use the techniques and routines described in [5] and especially Chapter 5 of [16]. In short, we use the deviation vector method for speed, but check select results using the slower but more robust Jacobian method. We also use the Jacobian diagnostic described in [5,16] to verify the correctness of the (rather complicated) Jacobian matrix (which in fact is generated by *Mathematica* directly from the equations of motion). As a result, we are confident that our values for the Lyapunov exponents faithfully describe the true dynamics of the system.

[4]The additional use of the freely available package OPTIMIZE.M [33] gives a factor of 5 increase in speed for the case at hand.

[1] S. Suzuki and K. Maeda, Phys. Rev. D **55**, 4848 (1997).
[2] J. Levin, Phys. Rev. D **67**, 044013 (2003).
[3] J. D. Schnittman and F. A. Rasio, Phys. Rev. Lett. **87**, 121101 (2001).
[4] N. Cornish and J. Levin, gr-qc/0207016.
[5] M. D. Hartl, Phys. Rev. D **67**, 024005 (2003).
[6] M. D. Hartl, Phys. Rev. D **67**, 104023 (2003).
[7] L. Blanchet, T. Damour, B. Iyer, C. Will, and A. Wiseman, Phys. Rev. Lett. **74**, 3515 (1995).
[8] L. Kidder, Phys. Rev. D **52**, 821 (1995).
[9] T. Damour and G. Schäfer, Nuovo Cimento Soc. Ital. Fis. **101B**, 127 (1988).
[10] P. Jaranowski and G. Schäfer, Phys. Rev. D **57**, 7274 (1998).
[11] P. Jaranowski and G. Schäfer, Phys. Rev. D **60**, 124003 (1999).
[12] T. Damour, P. Jaranowski, and G. Schäfer, Phys. Rev. D **62**, 084011 (2000).
[13] T. Damour, P. Jaranowski, and G. Schäfer, Phys. Lett. B **513**, 147 (2001).
[14] E. Poisson, Phys. Rev. D **57**, 5287 (1998).
[15] T. Damour, Phys. Rev. D **64**, 124013 (2001).
[16] M. D. Hartl, Ph.D. thesis, California Institute of Technology, 2003, http://etd.caltech.edu/etd/available/etd-05222003-161626/.
[17] C. M. Will, Living Rev. Relativity **4**, 4 (2001).
[18] A. Buonanno, Y. Chen, and T. Damour,(to be published).
[19] J. Levin, Phys. Rev. Lett. **84**, 3515 (2000).
[20] N. J. Cornish and J. Levin, Phys. Rev. Lett. **89**, 179001 (2002).
[21] N. Cornish and J. Levin, Phys. Rev. Lett. **78**, 998 (1997).
[22] P. C. Peters, Phys. Rev. **136**, B1224 (1964).
[23] A. Buonanno and Y. Chen (unpublished).
[24] L. Blanchet and B. Iyer, Classical Quantum Gravity **20**, 755 (2003).
[25] N. Cornish and J. Levin, Phys. Rev. D **68**, 024004 (2003).
[26] M. Miller and D. Hamilton, Astrophys. J. **576**, 894 (2002).
[27] L. Wen, Astrophys. J. **598**, 419 (2003).
[28] N. Cornish and J. Levin, Classical Quantum Gravity **20**, 1649 (2003).
[29] C. Moreno-Garrido, J. Buitrago, and E. Mediavilla, Mon. Not. R. Astron. Soc. **266**, 16 (1994).

[30] K. Martel and E. Poisson, Phys. Rev. D **60**, 124008 (1999).
[31] A. Buonanno and T. Damour, Phys. Rev. D **59**, 084006 (1999).
[32] A. Buonanno and T. Damour, Phys. Rev. D **62**, 064015 (2000).
[33] Mark Sofroniou, A Package for Code Optimization Using *Mathematica*, http://library.wolfram.com/infocenter/MathSource/3947/.
[34] W. H. Press, S. A. Teukolsky, W. T. Vetterling, and B. P. Flannery, *Numerical Recipes in C* (Cambridge University Press, Cambridge, England, 1992).
[35] J.-P. Eckmann and D. Ruelle, Rev. Mod. Phys. **57**, 617 (1985).